Spacecraft Discharge Electromagnetic Interference Coupling Models

A.J. Woods and E.P. Wenaas
JAYCOR, San Diego, California

Nomenclature

a = radius, m
A = area, m^2
B = magnetic induction, $=\mu H$; $Wb/m^2 = 1$ Tesla
c = speed of light, 3×10^8 m/s
C = capacitance, F
d = thickness, spacing; m
e = electron charge, 1.6×10^{-19} C
E = electric field, V/m
$\mathcal{E}$ = electron energy, eV
$\mathcal{E}_1$ = electron normal energy, eV
$\mathcal{E}_0$ = m_0c^2/e rest mass, 5.11×10^5 eV
f_B = fraction of stored charge which blows off
f_{stop} = fraction of electrons captured in a material
G = transmitted blowoff current rate of rise, A/s
h = height, m
H = magnetic field, A/m
I = current, A
j = $\sqrt{-1}$
J = current density, A/m^2
k = wave number ω/c, rad/m
ℓ,l = length, m
L = inductance, H
m = macroparticle mass, kg
m_e = electron mass, 9.1×10^{-31} kg
n = electron number density, No./m^3
N = neutral species number density, No./m^3
$\dot{P}$ = time rate of change of dipole moment per unit area, A/m
q = macroparticle charge, C
Q = total charge, C
r = distance, m
R = radius, m; resistance, Ω
R_r = radiative resistance, Ω
s = equivalent electrical circuit equation roots, s^{-1}
t = time, s
t_D = damping time, s
T_0 = ringing period, s
T_R = pulse rise time, s
T_W = pulse full width at half maximum (FWHM), s
v = electron velocity, m/s
v_p = discharge propagation velocity, m/s
V = volume, m^3; potential, V
W = energy, J
x,y,z = Cartesian coordinates, m
Y = admittance, Ω^{-1}
z,r,ϕ = cylindrical coordinates, m, m, rad, respectively
Z_0 = impedance of free space, 377 Ω
Z = impedance, Ω
α = aperture penetration shape factor (dimensionless)
γ = relativistic expansion factor, $1/\sqrt{1-(v/c)^2}$
δ = electromagnetic skin depth, m
Δt = time step, s
ϵ = dielectric permittivity, C^2/nm^2
ϵ_0 = permittivity of free space, 8.9×10^{-12} C^2/nm^2
η = electromagnetic shielding effectiveness (dimensionless)
λ = wavelength, space-charge-barrier dimension, m
μ_0 = permeability of free space, $4\pi\times10^{-7}$ n/A^2
ν = frequency, s^{-1}
ρ = charge density, C/m^3
σ = conductivity, mho/m
σ_i = electron-neutral ionization cross section, m^2
ω = angular frequency, rad/s

Subscripts

c = characteristic, as in characteristic impedance
d = discharge property

Andrew J. Woods was born in 1944 in Lodi, California. He received his B.A. in physics from the University of California at Berkeley in 1966 and his M.S. in physics from California State University at San Diego in 1969. In 1966 he was employed at the China Lake Naval Ordnance Test Station in California where he worked with experimental laser systems. From 1967 to 1976 he performed computer modeling of radiation transport and nuclear electromagnetic pulse phenomena (EMP) at Gulf General Atomic (later IRT Corporation). In 1976 he joined JAYCOR, where he has studied a variety of electromagnetic pulse phenomena, including a joint experimental/analytical spacecraft discharge electromagnetic coupling investigation sponsored by the Air Force Weapons Laboratory.

Eric P. Wenaas received his Ph.D. in applied physics from the State University of New York at Buffalo in 1969. He directed the Electro-magnetics Group at IRT Corporation and studied electromagnetic effects on spacecraft and missile systems. While IRT was a part of Gulf General Atomic, Dr. Wenaas was involved in basic research on particle interactions with solid surfaces. In 1976 he joined JAYCOR, where he is currently Senior Vice President in charge of the Radiation Effects Group, concerned with survivability, vulnerability, and hardening of electronic systems to effects of natural space and nuclear radiation. He has specialized in EMP, system generated EMP (SGEMP), and electron caused EMP (ECEMP), and has pioneered many of the SGEMP/ECEMP analysis and hardening techniques for spacecraft systems. Dr. Wenaas has published numerous articles on SGEMP and ECEMP and has authored over 100 technical reports and handbooks.

Received Oct. 19, 1984; revision received Jan. 18, 1985.

e	= emitted electron property
E	= relating to electric field
H	= relating to magnetic field
inc	= incident field property
L	= load, as in load resistance
nor	= normal field component
oc	= open circuit condition
p	= peak value
tan	= tangential field component
tr	= transfer, as in transfer impedance
z,r,ϕ	= cylindrical coordinate components
0	= initial or incident value

Introduction

SPACECRAFT in orbit can attain high differential voltages on and near dielectric materials due to both natural and nuclear electron environments. Breakdown and flashover thresholds can be exceeded and charge transported from dielectrics to the spacecraft and the surrounding volume. The motion of the charge is capable of inducing substantial electromagnetic fields and currents on the structure which can couple to electronics causing upset or burnout malfunctions.[1-3] The phenomenology associated with spacecraft dielectric discharge is widely known as electron-caused electromagnetic pulse (ECEMP).

There are two facets of the spacecraft charging problem which are closely related but, in general, can be decoupled from each other. The first involves the mechanism and location of charging, while the second involves the mechanisms and coupling models associated with the resultant discharges. The emphasis in this paper is on the discharges and the associated coupling. Descriptions of how the spacecraft charges are treated elsewhere.[4]

The objectives of this paper are to acquaint the reader with the spacecraft discharge electromagnetic interference (EMI) problem and to survey analytical and numerical models available for estimating the magnitudes of the unwanted signals. Emphasis is on the development of models with simple algebraic expressions useful for estimating worst-case responses. Methods for obtaining more accurate time- and frequency-domain data are described briefly, but the reader is directed to the references for details.

This article overviews the EMI problem which results from discharges on and throughout a structure. Then the source functions for various categories of discharges are characterized in terms of the fractions of stored charge released and the pulsewidths of the released charge. The blowoff charge from dielectric-covered surfaces has the most far-reaching impact, and methods for predicting its motion are discussed. Methods for calculating the electromagnetic fields generated by the charge motion are described, and generic paths and mechanisms for coupling the fields into electronics are discussed. Sample illustrative calculations are performed throughout the article, and compared with experimental data in some cases.

References to work performed in the associated fields of nuclear electromagnetic pulse (NEMP), system-generated electromagnetic pulse (SGEMP), and internal electromagnetic pulse (IEMP) are found throughout the discussion. These disciplines, along with lightning and electromagnetic compatability investigations on aircraft, missiles, and ground systems, provide a wealth of references pertinent to the satellite problem at hand.

Much of the theory and experimental data discussed herein were produced during an extensive laboratory program investigating dielectric discharges.[5-8] Various objects up to 1 m in size were charged to the point of spontaneous discharge with electron beams and the resulting electromagnetic responses measured. Analytic models and detailed numerical simulations of the various configurations and processes were constructed. It is recognized that laboratory-measured discharge characteristics are not in complete agreement either among various experimenters or with available data obtained in space (see section on "EMI Source Characterization"). This unfortunate condition does not affect the methods presented here, in which the discharge current source functions are treated as empirically derived input parameters. These parameters will no doubt be refined in subsequent efforts. The methods employed here should be applicable equally to natural and nuclear charging environments.

Spacecraft Discharge EMI Phenomenology

Figure 1 illustrates a spacecraft subjected to an incident electron environment. In general, electron environments of interest have the capability to both charge the outside of the spacecraft and penetrate deep into the interior[2,9] to charge internal dielectrics or isolated conductors. The entire structure may attain a high potential as a whole, and may also attain large differential potentials particularly when exposed to ultraviolet light from the sun. Thus, strong fields may result in and near dielectrics both external and internal due either to direct charging or spacecraft structure grounding effects. The fields can become sufficient to cause dielectric breakdown and its associated charge flow.

Figure 2 summarizes the spacecraft discharge and coupling for discharges which occur in each of the major geometrical divisions of a system. The diagram illustrates the relation between various discharge locations and the electronics box which is usually the point where EMI signals are of concern. Discharges occurring anywhere on the system can couple to the electronics box, or discharges can occur within the box itself as a result of charging by the high-energy portion of the incident electron spectrum which can penetrate directly into the box.[10] These latter discharges produce unwanted signals directly at the electronics, unattenuated by terminal protection devices, cable shields, or electromagnetically closed cavities as are discharges outside the box. In many cases, the magnitude and frequency of occurrence of these discharges can be greatly reduced compared to external discharges by the small size of the box and the substantial attenuation of the incident electron spectrum as it penetrates intervening materials. In general, the closer into a box a discharge occurs, the smaller its magnitude will be, but, on the other hand, the coupling of the unwanted signal from the point of discharge into the electronics will be larger. Figure 2 shows that the discharge current source functions must be characterized for external and internal surfaces, cables, and box interiors. The key structural and shield leakage parameters must be known so estimates of the signal coupling to the box may be made.

Some external discharge points are illustrated in Fig. 3 by the arrows representing electrons which flow off onto neighboring surfaces with lower potentials. Discharge points leading to large currents which may propagate over substantial

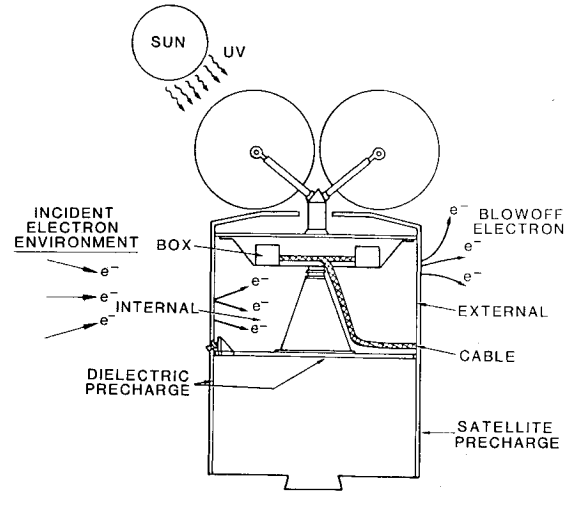

Fig. 1 Spacecraft charging phenomenology.

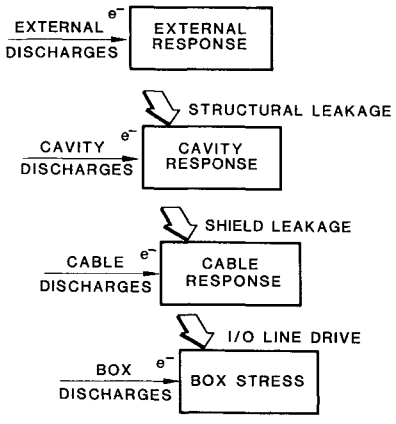

Fig. 2 ECEMP phenomenology relationships.

distances include thermal blanket blowoff onto neighboring antenna structures and blowoff to conducting portions of the centerbody. Discharges on solar cells may be important; however, for the example shown, the signals which reach important locations are not large based on the measurements and calculations of Ref. 5. Other external discharge points capable of causing substantial EMI signals include large telescope mirrors discharging to neighboring structural elements and nonconducting paints.[11,12]

Some internal discharge points are illustrated in Fig. 4. Cable dielectric jackets and internal blankets (typically found around propellant tanks) may discharge. EMI can result from direct collection or ejection of charge onto the cable surfaces. Coupling due to a rapidly changing electric or magnetic field may also be substantial and would not require direct space charge transfer to the vicinity.

Internal dielectrics in the cables themselves are capable of discharging, as illustrated in Fig. 4.[2] The mechanism is the accumulation of charge in the insulator from the high-energy portion of the spectrum. Depending upon the radiation-induced dielectric conductivity, the electric field across the insulator may or may not reach breakdown levels. The result of a discharge, if it should occur, is a flow of current across the dielectric intercepted by the center conductor causing EMI in the circuit.

Another source of discharges is isolated metal conductors both on the structure and on printed circuit (PC) boards within electronic boxes. Isolated metal conductors found on spacecraft include unused wires in cable bundles, ungrounded relays, unused lands on PC boards, PC board stiffeners, and spot radiation shields. These isolated conductors can charge until a spontaneous discharge occurs when the flux of penetrating electrons onto the conductor exceeds the leakage rate from the conductor through any contacting dielectic. This type of discharge can have severe consequences for spacecraft electronics, particularly when the isolated metal is in a cable bundle or on the PC board itself.

Characterization of EMI Source Functions

The purpose of this section is to characterize the EMI source functions resulting from three categories of discharges including blowoff, flashover, and punch-through (breakdown). "Blowoff" electrons are those which become free of the dielectric and propagate through space. Some of these may travel substantial distances and others may hug the surface of the discharging material, but they are free to move as electric (and magnetic) fields determine. In general, the greatest number of these electrons experience very short excursions away from the discharging surface due to space-charge limitation effects. Even though they are free, only a tiny fraction (less than 1%) may escape the vehicle by the end of a pulse. The majority never traverse more than a few centimeters from the edge or the discharging material.

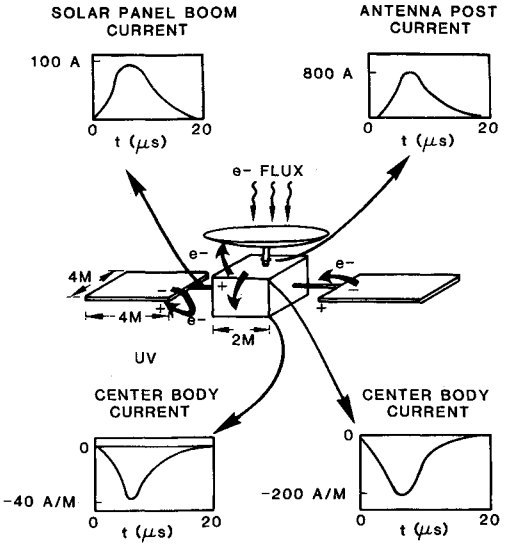

Fig. 3 Postulated spacecraft discharge response scenario based on scaled experimental measurements performed on 1-m sized objects in a monoenergetic 25-keV electron environment.[5] 2500 A are released from Mylar thermal blankets and 500 A are released from quartz on solar panels inducing the responses shown.

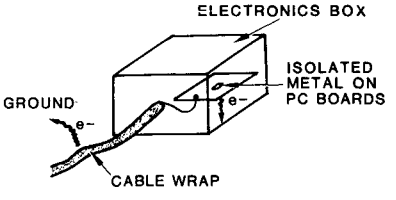

a) Dielectric cable wrap and isolated metal on PC board inside box discharging to ground

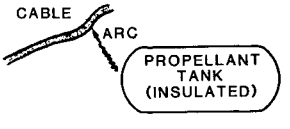

b) Insulated propellant tank discharging to cable shield

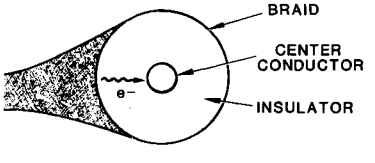

c) Cable interior dielectric discharging to center conductor

Fig. 4 Examples of potential internal discharge points.

"Flashover" electrons are those which are constrained to move across the surface to some discharge point at an edge or material penetration. These are not free to move into space as the blowoff electrons are, but are held by properties of the dielectric. "Punch-through" electrons are those which may penetrate through the body of the dielectric to the substrate. The microscopic behavior of electrons driving discharges is not well known, but from the evidence of Refs. 12-14 it is plausible that an electron can start out as a flashover particle until it reaches a discharge point and then becomes a blowoff particle. It seems probable that most punch-through electrons start out as flashover particles in the sense that they move across the surface in a constrained fashion to the discharge point.

In general, the blowoff current should be of greatest interest to the EMI analyst whether it occurs outside or inside a struc-

ture because it can propagate over substantial distances and induce fields over large areas. For cases of sandwiched dielectrics such as those that occur inside cables, the flashover/punch-through combination or volume breakdown is the charge which participates. Methods of estimating these sources are discussed below.

Blowoff vs Flashover and Punch-Through

Each of the three discharge processes has the capacity to induce strong replacement currents locally underneath the dielectric on the substrate. As charge propagates across or away from the surface, current flows on nearby conductors to replace it. The effects of the charge constrained to the immediate vicinity of the dielectric (punch-through and flashover) are essentially local, whereas the blowoff charge can be global. This point can be seen from the development in Ref. 15 which shows that for a small dipole (corresponding to a small simple arc discharge or "punch-through" through a thin dielectric on a sphere), the current I flowing at some distance r from a discharge point is

$$I = I_P d/r \tag{1}$$

where d is the dielectric thickness and I_P the peak current involved in the discharge. The discharge pulse duration is assumed to be long compared to object response times. Since $d \ll r$, for a typical system of interest, the replacement current due to confined charge motion falls off rapidly away from the point of discharge.

The restriction does not apply to the blowoff electrons, however. These particles are free to move in space as electromagnetic fields determine. An estimate of the extent of their trajectories early in a discharge pulse may be obtained by considering the distance traveled by an electron before the object charges to a potential sufficient to limit its path.

Suppose that electrons blow off a dielectric on one end of a conducting cylinder of radius R with a current density pulse rising linearly in time T_R to a peak value of J_p. J_p is the total emitted current density leaving the surface and does not include effects of space-charge limiting. If the initial differential voltage across the dielectric to the conducting substrate is V_0, then the electron trajectories will be limited once the body charges to that potential. (The conducting portion of the cylinder is assumed to have been initially at zero potential with respect to infinity due to some discharging process.) The body potential variation during the discharge is approximately

$$V = \frac{J_p R}{4\epsilon_0 T_R} \frac{t^2}{2} \tag{2}$$

until V_0 is reached. The effects of the electron cloud have been ignored for early time in determining the potential and the body capacitance is approximated by $4\pi\epsilon_0 R$ (ϵ_0 is the permittivity of free space). The time t_1 required to reach V_0 from the above expression is

$$t_1 = \sqrt{\frac{8V_0\epsilon_0 t_r}{J_p R}} \tag{3}$$

J_p can be related simply to V_0 by

$$J_p = \frac{Q_e}{A_e T_W} \tag{4}$$

where Q_e is the total charge emitted from area A_e with pulse full width of half maximum (FWHM) of T_W (typically the emission current pulse width is comparable to the risetime, T_R). Q_e has been empirically related to the total charge stored, Q_0, by a simple constant f_B for several spacecraft materials ($f_B < 1$, see "Blowoff Characteristics" section below).

Thus,

$$J_p = \frac{f_B Q_0}{A_e T_R} = \frac{f_B}{A_e T_R} \frac{\epsilon A_e}{d} V_0 = \frac{f_B \epsilon}{T_R d} V_0 \tag{5}$$

where d and ϵ are the dielectric thickness and permittivity, respectively. The pulse time T_R has also been empirically related to the dielectric's width (taken to be $2R$) by a material-dependent constant propagation velocity v_p by $T_R = 2R/v_p$. The space-charge limitation time is obtained by combining these relations:

$$t_1 = \frac{2}{v_p} \sqrt{\frac{8Rd}{f_B} \frac{\epsilon_0}{\epsilon}} \tag{6}$$

Before this time, a few of the electrons will move largely unhindered by fields. They are accelerated by the large differential potential to a terminal velocity of

$$v \simeq \sqrt{2eV_0/m} \tag{7}$$

(e/m is the charge-to-mass ratio for electrons). Consequently, they will move a distance $\ell \simeq vt_1/2$ away from the discharge site.

As an example of the considerable spatial extent of blowoff electron trajectories, consider a discharge using typical measured parameters. Kapton 2-mil thick has been observed to discharge at 13 kV when exposed to 25-keV monoenergetic electrons. It emits approximately one-third its charge as blowoff electrons ($f_B = 0.33$), and exhibits a discharge propagation velocity of $v_p = 1.8 \times 10^5$ m/s.[5] The time for a 0.45-m-radius object to charge to the observed discharge potential during a discharge and thus limit the blowoff charge is $t_1 \simeq 1.4 \times 10^{-7}$ s, where $\epsilon/\epsilon_0 = 3.5$ has been assumed. During this time, the electrons propagate a distance $\ell \simeq 4.7$ m. Both of these results are in reasonable agreement with detailed calculations and measurements made in the experimental series reported in Ref. 5 for Kapton on an isolated cylinder. The important point is that the distance is much greater than the dielectric thickness and, consequently, the signals from these electrons can be felt at a high level over a major extent of present-day spacecraft.

Even after space-charge limiting due to object chargeup occurs, the spatial extent of many of the blowoff electrons greatly exceeds the dielectric thickness. This is a consequence of the large accelerating potential available from the differential voltage which initiated the discharge. The electric field in this region far exceeds the opposing field due to the object chargeup, and continues to accelerate free electrons into space subject to limitations similar to those occurring in a vacuum tube (see Ref. 16). This behavior is illustrated in Fig. 5, which shows a numerical simulation of a Kapton discharge on the 0.45-m-radius object using the same parameters described previously. In the top figure, the electron cloud has not yet been entirely limited because the cylinder potential has not reached the initial differential potential across the dielectric. In the lower figure, the cylinder potential has reached the initial differential potential and, therefore, the electrons are prevented from moving to infinity but still travel substantially through space and along the cylinder.

For the case of a sandwiched dielectric the blowoff current does not exist, and the volume discharge becomes the important mechanism. It can have far-reaching impact by virtue of the electrical path connecting the electrodes. A cable dielectric breakdown inside the braid is an example of a potentially far-reaching transient. Source currents as high as 100 A/m of cable length are calculated for cables in Ref. 2 assuming that 100% of the stored charge participates in the discharge and all of the charge migrates to one conductor in 20 ns. However, the fraction which actually participates in a real cable geometry is not well known. Measurements have indicated that the cable response is one-fiftieth the value obtained using

the above assumptions for one cable type and electron charging environment (see the section on cable direct drive for additional details on this EMI source). The remainder of this section focuses on the blowoff charge source.

Blowoff Characteristics for Typical Materials

As discussed in the previous section, the electrons which induce strong signals on most major portions of structures are those which move free of the material and transport significant distances through space. These blowoff electrons have been quantified for several spacecraft materials with experiments using small, grounded substrate dielectric samples.[8,13] While it is not the intent of this article to treat the subject in detail, it is important to establish some of the blowoff charge properties based on laboratory experiments and acquaint the reader with apparent differences which exist between laboratory experimental measurements and those made in the actual space environment.

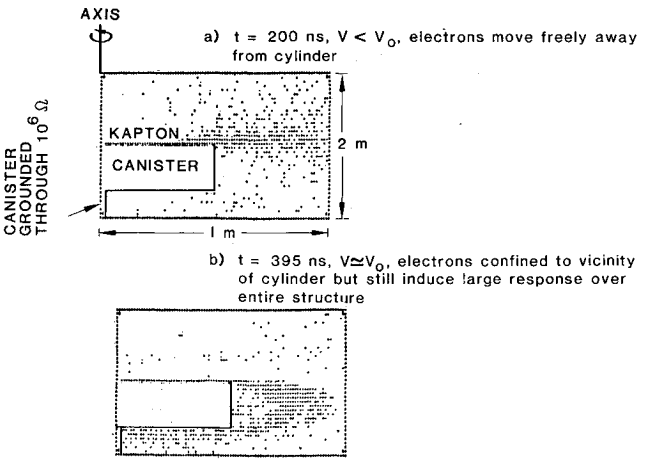

Fig. 5 Numerical simulation of an electron cloud at different times during a Kapton dielectric discharge on top of a high-impendance isolated cylinder. V is the instantaneous potential of the canister and V_0 the initial potential across the dielectric.

Based on laboratory measurements, blowoff electrons constitute between 20 and 90% of the total charge stored on a dielectric for typical spacecraft materials (see Table 1). They vacate the surface fairly uniformly, and their emission current pulse shapes and size-scaling relations suggest that the discharge propagates across the material with a characteristic velocity. Observed size-scaling relations of the blowoff charge properties are that the fraction of charge which participates is independent of sample size and the peak current and pulsewidth are proportional to the sample radius for samples as large as 1 m^2 in area and with approximately equal length and width. The parameters describing the discharge properties are fairly reproducible for successive discharges.

It is important to note that considerable uncertainty remains concerning discharge behavior vs environment. The data presented in Table 1 are for sample sizes approaching realistic satellite dimensions, but they are for a monoenergetic electron charging environment. Both the natural and nuclear charging environments contain a wide spectrum of electron energies, and laboratory efforts at simulating the spectrum have led to conflicting results so far. Treadaway et al.[10] found that discharges which occurred on Kapton samples in a monoenergetic 25-keV environment could be prevented entirely by the addition of a 100-pA/cm^2, 200-keV beam. On the other

Table 1 Discharge parameters for several satellite materials due to the 25-keV monoenergetic electron environment of an experiment[5]

Material	Kapton	Second-surface mirrors (SiO_2)	Mylar	Solar panel
Area, m^2	0.79	0.79	0.79	0.09
Thickness d mils	2	8	3	6
ϵ/ϵ_0	3.5	4.0	3.5	4.0
Potential at breakdown V_0, kV	13	6.5	11	7
Discharge propagation velocity v_p, m/s	1.8×10^5	6×10^5	3.3×10^5	6×10^5
Pulse rise time T_R, μs	5	1.5	1.3	0.75
Pulse width FWHM T_W, μs	5	1.5	3	0.75
Blowoff fraction of stored charge, f_B	33%	28%	90%	20%
Flashover fraction of stored charge, f_F	33%	18%	0	58%
Electron emission characteristics				
Peak current density J_p, A/m^2	510	180	1460	440
Total current I_p, A	400	140	1150	40
Current rate, A/s	8.1×10^7	9.5×10^7	8.8×10^8	3.5×10^7

Table 2 Comparison of combined low- and high-energy environments and induced discharge properties for two laboratory experiments

	Low-energy charging beam		High-energy charging beam		
	Energy	Current, nA/cm^2	Energy spectrum	Current, pA/cm^2	Results
Treadaway et al., 1979	25-keV monoenergetic	13	200-keV monoenergetic	100	Kapton discharges ceased altogether
Balmain and Hirt 1980	20-keV monoenergetic	10	Broadband S_R^{90} 0-2 MeV	5	Kapton and Mylar discharges increased in peak current by factors of ~2-3 compared to monoenergetic low-energy charging only

hand, Balman and Hirt[17] observed *enhanced* discharges on both Kapton and Mylar when they added a broadband S_R^{90} source to a environment similar to Treadaway's low-energy case. These results are summarized in Table 2. Thus, there is considerable uncertainty in the magnitudes of discharges which occur in realistic environments. Data from the SCATHA satellite experiments[18] show discharges at potentials considerably below those of the laboratory which further complicates the issue because the low potentials (≤ 1 kV) which were observed leave doubt as to whether EMI signals are sufficient to cause the damages which have been observed and heretofore attributed to them (see Ref. 1).

Simple Arc Model Description of the Blowoff Current

The simplest model of a dielectric discharge involves the representation of the charge separation which generates fields by a current filament which flows over a small distance with a specified pulse shape. The filament is a delta function in space with a time history typically taken to be quite simple. Attempts to fold in space-charge limitation effects on the charge motion can be made with a more complex pulse shape. Such a discharge representation may be quite realistic for a case in which charge flashes over the surface of a dielectric to a nearby ground separated by a small distance from the charge surface. The arc also can be used less exactly to represent a more complex cloud such as that shown in Fig. 5. Examples of this simplest of blowoff models are found in the next and following sections.

Generation of Electromagnetic Fields

Electromagnetic fields radiated around a spacecraft due to a discharge can be estimated from the source currents by analytical and numerical methods. A disadvantage of the analytic method is that the source must be quite simple, and the body interaction is either not included or greatly simplified. Numerical treatments which solve Maxwell's or Poisson's equations consistently with particle charge motion can predict complex geometry effects self-consistently with electron clouds, but may have the disadvantage of requiring considerable computer modeling and resources. A simplifying assumption which can often be employed to reduce computer requirements is the quasistatic approximation. This approximation may be permissible due to the long discharge pulse lengths. Also, complex structural details can be modeled with an equivalent circuit using blowoff currents and fields as drivers for an economical (and, in many cases, illuminating) calculation.

Analytic Fields for a Simple Arc Discharge

Based on the development in Ref. 19, the fields radiating outward from an arc in free space are

$$E_z = \frac{h}{4\pi}\left(\frac{\mu_0 \dot{I}}{r} + Z_0 \frac{I}{r^2} + \frac{Q}{\epsilon_0 r^3}\right) \tag{8}$$

$$H_\phi = \frac{h}{4\pi}\left(\frac{\dot{I}}{rc} + \frac{I}{r^2}\right) \tag{9}$$

where the arc flows with current $I(t)$ for a small distance h and the fields are evaluated in the plane normal to the current flow and a distance r from it. Q is the time-integrated current, $Z_0 = \sqrt{\mu_0/\epsilon_0} = 377\ \Omega$ the intrinsic impedance of free space, and c the speed of light. If the discharge occurs near the surface of a conductor and the fields radiate along it to penetration points of interest, then the above values should be multiplied by two due to reflections from the surface.

Self-Consistent Electromagnetic Fields

Electromagnetic fields from either complex current source functions or complex geometries must be obtained numerically. Typical calculations involve the use of standard compute codes developed for SGEMP or IEMP applications.[20-22] These compute electric and magnetic fields in the time domain given the currents for two- and three-dimensional geometries. Both electromagnetic and quasistatic approaches have been employed. The latter approach may be accomplished either mathematically in the computer model or by conducting an electromagnetic calculation to a series of steady-state solutions for different source current distributions corresponding to different times in the pulse and then constructing a response time history by piecing together the solutions at each instant. Both of these approaches—quasistatic and electromagnetic—have been employed in the arbitrary body of revolution code (ABORC)[22]; described briefly below to acquaint the reader with the numerical methods. ABORC has been perhaps the most widely employed computer code of its type in SGEMP/IEMP/ECEMP problems and therefore, represents the methods well. Variations on ABORC-type methods employed by others are generally performed in the interest of saving computer time while preserving the essentials of the physical modeling. Particularly helpful in this respect for the present problem is the use of virtual cathode emission to reduce the number of macroparticles which must be followed.[23]

Description of the ABORC Code

ABORC is designed to solve Maxwell's equations by direct finite differencing for axisymmetric geometries. Spatial current densities are obtained from finite "particles" of charge which are followed through the spatial mesh of zones. Each particle represents many negative or positive charges and is acted on by the local electric and magnetic fields during each time step. Emission of arbitrary energy, angular, spatial, and time distributions of currents can be specified. The calculational volume may contain either conductors or vacuum, with variable conductivity, permittivity, and permeability (σ, ϵ, μ).

The electromagnetic field equations are solved on a cylindrical coordinate system (z, r, ϕ):

$$\frac{-\partial H_\phi}{\partial z} = J_r + \dot{D}_r + \sigma E_r \tag{10}$$

$$\frac{\partial H_r}{\partial z} - \frac{\partial H_z}{\partial r} = J_\phi + \dot{D}_\phi + \sigma E_\phi \tag{11}$$

$$\frac{1}{r}\frac{\partial}{\partial r}(rH_\phi) - \frac{\partial H_r}{\partial \phi} = J_z + \dot{D}_z + \sigma E_z \tag{12}$$

$$-\frac{\partial E_\phi}{\partial z} = \mu \dot{H}_r \tag{13}$$

$$\frac{\partial E_r}{\partial z} - \frac{\partial E_z}{\partial r} = \mu \dot{H}_z \tag{14}$$

$$\frac{1}{r}\frac{\partial}{\partial r}(rE_\phi) = \mu \dot{H}_z \tag{15}$$

E is the electric field, H the magnetic field (equal to B/μ, where B is the magnetic induction and μ the permeability), $D = \epsilon E$ the displacement current density, ϵ the permittivity, J the spatial current density, and σ the conductivity. The terms which reference E_ϕ, H_z, or H_r allow for the effects of the geomagnetic field.

The above equations are computed on grids which are input to the code. Experience has shown that reasonable agreement with available experimental data can be obtained with 1-cm zones above dielectric surfaces where blowoff electrons emanate. This zone size is typically employed in calculations,

and an artificially high permittivity is used for the dielectric region to represent its capacitance properly. A typical value for this permittivity is $\epsilon \simeq 1000$.

In addition to Maxwell's equation subroutine, ABORC has a Poisson equation solver from which electrostatic fields may be obtained at each time step. This routine employs an iterative scheme for convergence at each new step starting with the fields from the previous step and the particle charge density from the new step. It allows reasonably fast simulation of actual dielectric thicknesses (on the order of mils) which would be impractical with the Courant condition limitations which exist on the full set of Maxwell's equation. The fine zone capability also allows for determination of peak fields in regions of sharp gradients.

The emitted charge representing blowoff electrons is accumulated into particles emitted from spatial zones on the dielectric. These move about in the electromagnetic fields according to the following equations of motion:

$$v_z^+ = v_z + \frac{q\Delta t}{m\gamma}(E_z + v_r B_\phi - v_\phi B_r) \tag{16}$$

$$v_r^+ = v_r + \frac{q\Delta t}{m\gamma}(E_r + v_\phi B_z - v_z B_\phi) \tag{17}$$

$$v_\phi^+ = v_\phi + \frac{q\Delta t}{m\gamma}(E_\phi + v_z B_r - v_r B_z) \tag{18}$$

$$\gamma^+ = \gamma + \frac{q\Delta t}{2mc^2}\{E_z(v_z^+ + v_z) + E_r(v_r^+ + v_r) + E_\phi(v_\phi^+ + v_\phi)\} \tag{19}$$

where the superscript + denotes values at the end of the time step. Terms in the equations which treat the geomagnetic effects are those referencing E_ϕ, B_z, and B_r. Also, the substitution $\vec{B} = \mu\vec{H}$ has been employed. γ is the rest mass relativistic expansion factor, v the particle velocity component, q the particle charge, m the particle mass, and Δt the time step.

The response calculations begin in the presence of static fields due to an initial charge on the dielectric. The static fields are obtained by separate calculations in which a charging current is specified across the dielectric model and/or between the structure ground and infinity. The fields correspond to a uniform charge density across the sample; an assumption previously validated for ideal conditions.[5] Other charge distributions can also be specified as appropriate.

The physics of the discharge process is modeled in the calculations to the degree that the discharge electron release rate, spatial and energy distributions, and dielectric charge reflection properties are specified. These quantities are independent inputs to the calculations, not the results of atomic physics modeling. A more detailed model, including atomic physics of the dielectric, could be incorporated if one becomes available. In calculations made to date with ABORC, only parameters empirically determined from measurements on small samples have been employed as electromagnetic response drivers.[8] Typical values employed in the calculations are representative of large discharges observed in experiments (see Table 1).

The ABORC discharge model employs uniform spatial emission, a triangular time history, and essentially zero initial electron kinetic energy. Flashover currents enter the calculations to the extent that the potential across the sample varies with time due to both blowoff and flashover effects. The charge motion is computed self-consistently which causes the emitting dielectric to become essentially a cold-electron-emitting cathode by virtue of the generally employed perfectly reflecting properties of the dielectric surface model.

ECEMP calculations are generally conducted assuming a perfect vacuum about the system. There is some evidence to suggest that plasma emissions may accompany the blowoff process,[5,14,24] and these may be modeled in the code. However, these inputs are not well known and, therefore, generally are treated parametrically, i.e., the various neutral and plasma species number densities are specified based on "evidence" rather than direct measurements of the quantities, and then the calculated response of the structure is compared with measurements to see if the behavior is described better with a plasma than without.

When ionization of neutral species and plasma effects is modeled, the code emits new particles representing ionization products when the calculated charge buildup in a zone due to ionization reaches some predetermined electron density. Specifically, a particle is emitted in a cell due to ionization when

$$N\iint \frac{dn}{d\mathcal{E}}\sigma_i v\, d\mathcal{E}\, dt \geq n_e \tag{20}$$

where n_e is an input parameter, $dn/d\mathcal{E}$ the energy spectrum of electrons (number per unit volume per unit energy) in each zone, v their velocity, N the neutral number density, and σ_i the electron-neutral ionization cross section of neutral species which may be ejected from the dielectric. The emitted electron is assumed to have zero initial energy and leaves behind a stationary ion. The value of n_e is chosen by a simple criterion which optimizes code efficiency based on the ability of the generated secondaries to modify the object response:

$$n_e \simeq 2H/evR \tag{21}$$

where H is the object magnetic field without a plasma present (pure vacuum), and v the incoming plasma electron velocity. This latter quantity can be estimated from a knowledge of the object potential in vacuum using Eq. (7).

Effects of the geomagnetic field are modeled with the field along the axis of the cylindrical coordinate system due to rota-

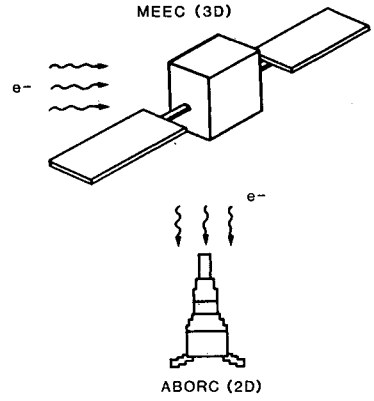

COMPUTATIONAL APPROACH

- MULTIDIMENSIONAL, FINITE DIFFERENCE E, H FIELDS
- ELECTRON EMISSION ENERGY AND ANGULAR DISTRIBUTIONS
- SELF-CONSISTENT MACROPARTICLE MOTION USING LORENTZ FORCE EQUATIONS
- FREE SPACE OR TANK BOUNDARY CONDITIONS
- TELESCOPING ZONES FOR STRUCTURAL DETAIL

PRACTICAL CONSTRAINTS

- ZONES 1 cm - 1 m, 1,000 - 170,000
- MACROPARTICLES - 1,000 - 300,000
- MACRO/MICRO DIMENSIONS - 100:1 RATIO
- TIME STEPS - 200 - 5,000 (LIMITED BY COURANT CONDITION)
- PROBLEM TIMES - 30 - 1,000 ns (LONGER FOR QUASISTATIC ASSUMPTION)

Fig. 6 Features of two numerical codes developed for SGEMP problems which have been employed to model ECEMP.

tional symmetry requirements in the code. The simulations begin with a constant value for the geomagnetic field B_{ez} everywhere in the grid at time zero. As particles gradually pick up a net azimuthal velocity, a magnetic field is generated in the direction opposite to B_{ez}. In general, the opposing field is spatially dependent. Hence, the particle motion and fields are calculated "self-consistently."

Boundary conditions for the ABORC code require the specification of an outer, perfectly conducting cylinder. Free-space solutions can be obtained by moving the outer boundary out and invoking an impedance matching scheme near the outer cylinder such that the transverse impedance is 377Ω. Finite conductivities can be specified representing imperfect conductors, and dielectric structures and high-permeability regions may be treated. Backscattering of electrons can be specified where charge is re-emitted from surfaces upon contact.

The code is dimensioned for a large number of spatial zones (typically 6000, but up to 25,000 may be employed). These cells may vary in size allowing fine object geometric detail. Numerous conducting regions for specification of bodies of revolution can be employed. Randomizing techniques are used for electron emission distributions. A virtually unlimited number of particles may be tracked during any given time step for as many time steps as desired. A typical number is ~10,000 simultaneously for an ECEMP discharge simulation. The code is written in FORTRAN, and computer times vary from 3 to 600 min on the CDC 7600 (or approximately five times longer on the CDC 6600) for full ECEMP discharge pulse simulations.

The basic approach used in ABORC and its three-dimensional equivalent, MEEC,[20] is summarized in Fig. 6. Some of the practical constraints relating to computer limitations are also listed in the figure. Additional details on numerical modeling of ECEMP problems are found in Refs. 5, 7, 25, and 26.

Example ABORC Calculation Compared with Experimental Data

Figure 7 shows a comparison between the ABORC-calculated and experimentally measured external response of a 1-m cylinder with second-surface mirrors discharging on the top. The mirrors were charged with a 25-keV electron source in a large tank.[5] ABORC input parameters are those described in Table 1. Agreement between the code and measurement is quite reasonable, and both support the theoretically tractable hypothesis that the blowoff electrons cause large cylinder response over significant distances. Based on the reasonably good agreement shown, it is thought that discharge effects are being modeled properly at least for simple geometries.

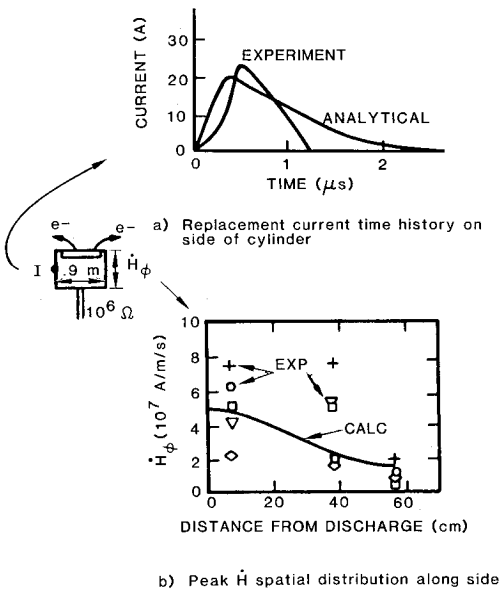

Fig. 7 Comparison of ABORC calculation and experimental measurement for the external response of a high-impedance-isolated cylinder with second-surface-mirror discharges on the top.

Equivalent Circuit Modeling for Complex Structural Response

The simple arc model and the self-consistent modeling above can give estimates of the EMI fields and currents which sweep across an object; however, if the structure is sufficiently complex it may be desirable to represent it as an equivalent circuit using the blowoff current as a driver. The basic approach is to assume that the discharge current source and structure are decoupled, and to input the net current or voltage from the discharge based on independent calculations as a source to the equivalent circuit of the structure. Two examples of this method are provided in the following. One is the ringing excited on a highly resonant structure, and the other is the coupling to an interior cavity. In the latter case, experimental data and detailed calculations are available for comparison with the results.

Resonant Structure

As an example of the equivalent circuit technique, consider the relatively complex three-axis-stabilized satellite geometry of Fig. 3. A model of this vehicle is illustrated in Fig. 8 along with the resultant boom current response computed with the MEEC-3D code for a symmetric, fast-pulse excitation. In this case, "symmetric" refers to the emission current being symmetric about a plane which is perpendicular to the satellite major axis and which bisects the (supposedly symmetric) centerbody. Such an excitation of a similarly symmetric structure will result in currents which flow equally and oppositely on each boom. The boom current shown exhibits a peak value similar to the peak replacement currents which flow on the centerbody, but has a strong resonant behavior which damps out slowly as radiation flows off into space. A real satellite might exhibit faster damping due to finite impedances of interconnecting materials, however, this calculation was performed assuming perfectly conducting interconnects. This situation probably best respresents real resonant vehicles which are typically grounded with high-quality connections everywhere so that radiation damping is the predominant energy-loss mechanism. In this section, a means of estimating the peak response, characteristic frequency, and damping rate for the symmetric and asymmetric modes of a resonant structure is provided.

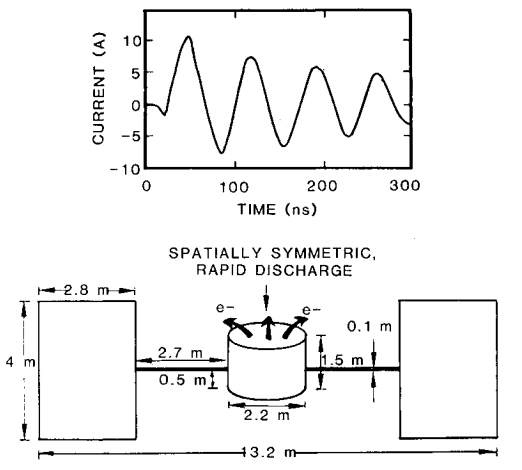

Fig. 8 Resonant satellite model and boom current response for a spatially symmetric fast-pulse excitation computed with the MEEC-3D code.

The external electrical characteristics of a resonant satellite can be represented by the simplified equivalent circuit shown in Fig. 9. C represents the capacitance of the solar paddles and centerbody, L the inductance of the booms, and R_r the radiative resistance. These elements have values which depend on the characteristics of the excitation of the structure represented by the current I_0. For a given excitation, the response can be represented by

$$I = I_0 \cos(\omega_0 t) e^{-t/t_D} \tag{22}$$

which is also the solution of the simple circuit. In the expression above, ω_0 is the frequency and t_D the damping time of the mode.

The current I_0 may be estimated by

$$I_0 = C_2 \dot{V} \simeq C_2 V_0 / t_1 \tag{23}$$

where C_2 is the centerbody capacitance to infinity, V_0 the potential at breakdown, and t_1 the time required for the centerbody to charge from zero to V_0 [Eq. (6)].

In the symmetric mode current flows equally and oppositely on each boom. The excitation magnitude I_0 can be reasonably approximated as one-half the value described above. The frequency of oscillations is

$$\omega_0 = 1/\sqrt{LC} \tag{24}$$

$$L = \frac{\mu_0 \ell}{2\pi} \ell n(\ell/a) \tag{25}$$

$$C = \frac{C_1 C_2}{C_1 + C_2} \tag{26}$$

where ℓ is the length of the high-inductance segment of the boom of radius a. C_1 and C_2 are the capacitances to infinity of one paddle and one-half the centerbody, respectively. Assuming these bodies do not affect each other's capacity strongly, estimates for C_1 and C_2 can be made with $C_1 = 4\pi\epsilon_0 b_2$ and $C_2 = 4\pi\epsilon_0 b_2$, where b_1 and b_2 are the radii of spheres with areas equal to one-half the centerbody and one paddle (both sides), respectively. L is the inductance of one boom in this mode. The damping time is $t_D = L/R_r$, where $R_r = 20(\omega_0 \ell / C)^2$ is the radiation resistance (Ω). The radiative resistance expression is for a current element of length ℓ in free space.

The asymmetric mode is also important. This is the mode in which current flows from one paddle through both booms and the centerbody to the other paddle. The same circuit model and element formulas apply as for the symmetric model, but the capacitances should be doubled corresponding to both paddles and the total centerbody. The boom inductance should also be doubled, and the radiative resistance term computed using the doubled boom length and the lower characteristic frequency, ω_0. Thus, we expect an oscillation approximately one-half as fast as the symmetric case, and having a slower damping rate. The total current of the centerbody should be used for I_0 in this case.

As a test of the algorithms, consider the symmetric satellite response of Fig. 8. Intermediate parameters required by the simple formulas are $L = 2.2 \times 10^{-6}$ H obtained with a boom length of 2.7 m and a radius of 0.05 m, and the centerbody and solar paddle capacitances $C_1 = 1.5 \times 10^{-10}$F and $C_2 = 8.1 \times 10^{-11}$F obtained with equivalent spherical radii of $b_1 = 1.3$ m and $b_2 = 0.7$ m, respectively. This results in total capacitance $C = 5.3 \times 10^{-11}$F, and a fundamental ringing frequency of $\omega_0 = 9.3 \times 10^7$ rad/s.

The period is $T_0 = 2\pi/\omega_0 = 68$ ns which compares favorably with the 70-ns period of Fig. 8. The damping rate time constant is $t_D = 1.6 \times 10^{-7}$s based on a calculated radiative resistance of $R_r = 14\Omega$. The damping rate of Fig. 8 is $\sim 2.5 \times 10^{-7}$ by inspection. Thus, the quantities are within a factor of 2 agreement with the three-dimensional code results for the symmetric mode. Other comparisons not reported here have shown similar agreement for the asymmetric case.

Cavity Inside a Cylinder with a Gap

In the laboratory experiment series involving discharges on 1-m sized objects,[5] a case was monitored in which the ECEMP fields could leak into an interior cavity in a controlled manner. The geometry is illustrated in Fig. 10 which shows a rotationally symmetric representation of the test body simulated in detail by ABORC. The actual test object was rotationally symmetric except for the placement of four 1-Ω resistors in the gap symmetrically spaced to simulate a representative satellite gap resistance.

In the ABORC simulation the calculated fields in the cavity changed much more slowly than the external fields and currents, and there was no cavity oscillation. The following simple equivalent-circuit analysis was performed in an attempt to explain these results and to predict the maximum cavity fields.

The equivalent circuit is shown in Fig. 10b, where L is the inductance of the centerpost ($\sim 2 \times 10^{-7}$H), C the capacitance of the structure below the gap to the structure above the gap [the vertical side of the cylinder actually contributes the major portion of the capacitance ($C \simeq 1.5 \times 10^{-10}$F)] $R = 0.25\Omega$ for four 1-Ω resistors in parallel, I_d the portion of the current emitted from the top of the cylinder during discharge which impinges on the exterior of the cylinder below the gap (available from ABORC).

The differential equation for current I_1 up the centerpost is

$$\frac{d^2 I_1}{dt^2} + \frac{1}{RC}\frac{dI_1}{dt} + \frac{2}{LC} I_1 = \frac{1}{LC} I_d \tag{27}$$

The two roots of this equation are

$$s_{1,2} = 0.5\left[-\frac{1}{RC} \pm \sqrt{\left(\frac{1}{RC}\right)^2 - 4(1/LC)}\right] \tag{28}$$

For the estimated values of R, L, and C, $RC = 3.75 \times 10^{-11}$ s and $LC = 3 \times 10^{-17}$ s^2. Since $(1/RC)^2$ is so much larger than $4/LC$, the two roots are approximately

$$s_1 \simeq -1/RC = -2.66 \times 10^{10} \text{s}^{-1} \tag{29}$$

and

$$s_2 \simeq -R/L = -1.25 \times 10^6 \text{s}^{-1} \tag{30}$$

Note that both roots are real; therefore, the system is overdamped and there is no oscillation of the cavity mode, in agreement with the ABORC simulation and experimental results. To achieve an oscillatory condition, R would have to be greater than 20Ω.

If the current driver I_d increases linearly from zero at $t = 0$ (i.e., $I_d = Gt$), the equation for I_1 during the linear increase of I_d is

$$I_1 = G\left[\frac{(1 + s_2 L/R)}{(s_2 - s_1)} \exp(s_1 t) - \frac{(1 + s_1 L/R)}{(s_2 - s_1)} \exp(s_2 t) + t - L/R\right] \tag{31}$$

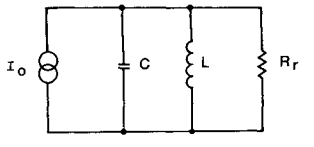

Fig. 9 Lumped-element resonant satellite equivalent circuit representation including radiative resistance.

Remember that s_1 and s_2 are negative quantities.

The coefficient in front of $\exp(s_1 t)$ is very small and the exponential decays very rapidly. Hence, this term can be ignored. Moreover, the coefficient of the second exponential is essentially L/R. Hence, the approximate expression for I_1 is

$$I_1 \simeq Gt - L/R[1 - \exp(s_2 t)] \tag{32}$$

For $t \ll -1/s_2 = L/R = 0.8$ μs, the exponential is approximately

$$\exp(s_2 t) = \exp(-Rt/L) \simeq 1 - Rt/L + \tfrac{1}{2}(Rt/L)^2 \ldots \tag{33}$$

Substituting into Eq. (32) only the t^2 terms remain, so I_1 increases initially as a slow quadratic of t.

For $t \gtrsim -3/s_2 = 2.4$ μs, the exponential becomes negligible, and

$$I_1 \simeq G(t - L/R) \tag{34}$$

If the driver current I_d is triangular with its peak at 5×10^{-6} s, which is approximately the value for Kapton in this geometry, the current up the post at the time of the peak I_d is

$$\frac{t - L/R}{t} = \frac{5 - 0.8}{5} = 84\% \text{ of the peak driver current.}$$

In other words, although the current in the post starts to rise quite slowly, eventually it becomes a large fraction of the full driver current for the circuit parameters used here.

For second-surface mirrors, the time to peak I_d is only about 0.8 μs, therefore, the $\exp(s_2 t)$ term in Eq. (1) has not decayed completely at the time of the peak current. Using $s_2 t = -1.0$, the current in the centerpost at the time of the peak I_d would be about 0.37 $I_{d\text{peak}}$. However, the peak post current actually occurs somewhat after the peak I_d, therefore, its magnitude is estimated to be about 0.5 $I_{d\text{peak}}$.

From these results one can estimate the magnitude of the electric and magnetic fields inside the cavity. For second-surface mirrors, assume a peak $I_d = 140$ A at 0.8 μs based on the assumption that the peak emission current (Table 1) from the dielectric transports through space across the nearby gap (see Figs. 5 and 7). Therefore, for a triangular pulse, $G = 1.8 \times 10^8$ A/s. The voltage across the gap, by summing voltage around the loop in Fig. 10, is

$$V = L\frac{dI_1}{dt} \tag{35}$$

Differentiating Eq. (32), the value of dI_1/dt at $t \simeq 0.8$ μs is

$$\frac{dI_1}{dt} \simeq G[1 + L/Rs_2 \exp(s_2 t)] = 1.5 \times 10^8 \text{A/S} \tag{36}$$

and $V_{\text{peak}} \simeq 30$ V.

The maximum electric fields in the cavity will be near the gap. For a gap width of 1.5 cm, this field is 20 V/cm. Near the bottom of the cavity, the electric field normal to the cavity walls would be comparable to the voltage V divided by the length of the post (~ 35 cm), giving an electric field of about 1 V/cm. At a point $a = 5$ cm from the canister centerline, the peak $\dot{B}$ is

$$\dot{B} = \mu_0 \dot{H} = \frac{\mu_0 \dot{I}_1}{2\pi a} = 600 \text{ Tesla/s} \tag{37}$$

At points farther from the post, $\dot{B}$ decreases approximately as $1/R$.

Oscilloscope photos for a second-surface mirror discharge shown in Ref. 5 indicate a peak post current rate of rise value of about 7×10^7 A/s which is one-half the peak value estimated above for $\dot{I}_1$. The resistor traces indicate gap voltages of 5-7 V, again somewhat lower than the estimated values. Overall, the agreement among the models and data is encouraging, especially when one considers the stochastic nature of the discharges.

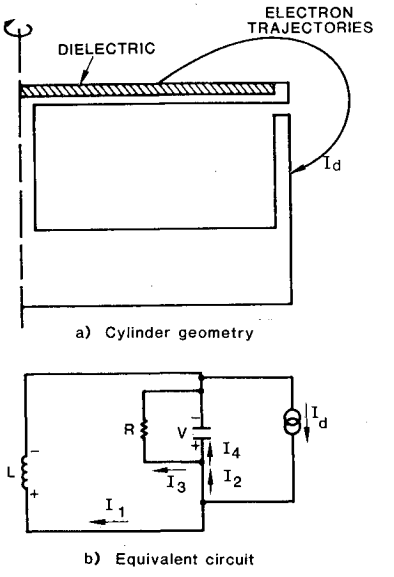

Fig. 10 Geometry and equivalent circuit for cavity responses calculated and measured in a laboratory experiment series conducted on 1-m sized objects.

External Field Penetration to the Interior

Mechanisms for the penetration of the large external fields to internal cavities are various apertures, screens, gasketed panels, and partially conducting surfaces. This subject has undergone intense investigation for more than a decade, and there is much literature available for various geometries relating to satellites, missiles, airplanes, and ground systems. In the following, an attempt is made to extract a few key results from the literature for simple cases in order to permit estimation of effects and some understanding of the phenomena. Detailed results including complex near-resonance effects are found in the references.

The focus of this section is on the analytical estimation of electromagnetic leakage through satellite structures. The approach may have some usefulness in the absence of experimental data for field coupling, but for realistic systems it is largely inadequate due to the great complexities of satellite geometries. A subsequent section discusses experimental transfer functions briefly. These are relied upon in serious investigations.

Penetration Through Apertures

The subject of field penetration through apertures is treated in some detail in Refs. 27-30. From those studies it is concluded that a small aperture (compared to the incident electromagnetic wavelength) in a finite body can be treated reasonably by the same size hole in an infinite sheet. Expressions for the fields behind an elliptical aperture in an infinite sheet obtained from Ref. 30 are:

$$\frac{E_x(x,0,z)}{E_{\text{nor}}} = -\frac{\alpha_E \ell_1^3 xz}{r^5}, \qquad \frac{H_y(x,0,z)}{E_{\text{nor}}} = -\frac{\alpha_E \ell_1^3 jk_0 x}{480\pi^2 r^3} \tag{38}$$

$$\frac{E_x(x,0,z)}{H_{\tan}} = \frac{30\alpha_H \ell_1^3 jk_0 z}{r^3}, \qquad \frac{H_y(x,0,z)}{H_{\tan}} = \frac{\alpha_H \ell_1^3}{4\pi r^3} \tag{39}$$

$$r = \sqrt{x^2 + z^2} \tag{40}$$

E_{nor} and H_{tan} are the fields incident normally and tangentially to the plane of the aperature, respectively, $k_0 = \omega/c$ the wave number, and $j = \sqrt{-1}$. These are the fields which would have been there without the aperture present. The shape factors α_H and α_E are functions of the ellipse aspect ratio and are given in Fig. 11. Note the static $1/r^3$ dependence of the principal field components (E_x/E_{nor}, H_y/H_{tan}) near the aperture, and the frequency independence of the principal components; pulses pass through the aperture with little distortion. It should also be noted that internal fields are proportional to ℓ_1^3 so that doubling the size of an aperture would result in an eight-fold increase in the interior fields.

Penetration Through Screens

Large apertures may be covered with a screen for reducing unwanted electromagnetic signals inside. The shielding effectiveness η_H^0 and η_E^0 (defined as the ratios of transmitted to incident magnetic and electric fields) of such a screen can be estimated from a simple formula for an electric field normal to the plane of the screen found in Ref. 27. For $\lambda \gg d$, where λ is the pulse wavelength and d the grid spacing

$$\eta_H = \eta_E^0 \simeq 2/(2 + Y_s Z_0) \tag{41}$$

$$Y_s = \left[\frac{\omega\mu_0 d}{2\pi} \ell n\left(\frac{d}{2\pi a}\right)\right]^{-1} \tag{42}$$

where Y_s is the equivalent sheet admittance and a the wire radius.

As an example calculation, consider the shielding afforded by a 1-cm mesh of 0.5-mm-radius wires for an ECEMP discharge of pulsewidth $T_W = 200$ ns. Allowing that $\omega \simeq \pi/2T_W$, the equivalent sheet admittance is $Y_s \simeq 50\Omega^{-1}$. The effective shielding is $\eta \simeq 1.1 \times 10^{-4}$ or $\simeq 79$ dB. Such a screen affords considerable protection against a typical ECEMP pulse.

Penetration Through Gasketed Panels

Penetration through gasketed panels is discussed analytically in Ref. 27 and experimentally in Ref. 31. The experimental results are presented for a variety of gasketed arrangements. From that investigation it was concluded that the transfer impedance is a more important coupling mechanism (magnetic field) than the transfer admittance mechanism (electric field). The approximate worst-case impedance Z_{tr} found was 0.1 Ω/cm of gasket periphery at 1 M Hz for the materials tested, and the values varied linearly with frequency in most cases across the entire range of interest for ECEMP: $Z_{tr} = 0.1\ \nu/\nu_0 \Omega$/cm for 0.1 M Hz $\leq \nu \leq$ 100 M Hz, $\nu_0 = 1$ M Hz. The total transfer impedance times the current flowing across the gasketed panel gives the open-circuit voltage on conductors inside. The panel was a standard 20×20 cm square fastened by eight screws.

As an example calculation, consider the voltage induced on a conductor behind the $\ell = 20$ cm square panel for the second-surface mirror discharge on the 0.9-m-diam cylinder shown in Fig. 7. The peak replacement current measured halfway down the cylinder was $I = 23$ A with a pulse width $T_W \simeq 0.5$ μs. This corresponds to a magnetic field of $H = I/2\pi R \simeq 8$ A/m and a frequency $\nu \simeq 1/(4T_W) = 0.5$ M Hz. The panel transfer impedance at this frequency is $Z_{tr} = 0.05$ Ω/cm. The periphery of the panel is 4 ℓ and the induced voltage on the conductor is

$$V = HZ_{tr} 4\ell^2 \simeq 6\text{V} \tag{43}$$

Penetration Through Imperfectly Conducting Sheets

A likely penetration path for external discharge signals is straight through conductively coated thermal blankets which may cover large yawning cavities. These fields are attenuated by the conducting layer, typically aluminum, according to the skin depth δ and thickness d:

$$H = H_0 e^{-d/\delta} \tag{44}$$

where H_0 is the external magnetic field and H the internal field. δ may be estimated by

$$\delta = \sqrt{\frac{2}{\omega\mu\sigma}} \simeq \sqrt{\frac{1.3T_W}{\mu\sigma}} \tag{45}$$

where T_W is the magnetic field pulsewidth and μ and σ the permeability and conductivity of the conducting layer. Assuming $T_W = 200$ ns, the skin depth is $\delta \simeq 7.3 \times 10^{-5}$m. This depth is much greater than the typical aluminized layer thickness of a few hundred angstroms. Consequently, the discharge fields can propagate virtually unattenuated through the blanket.

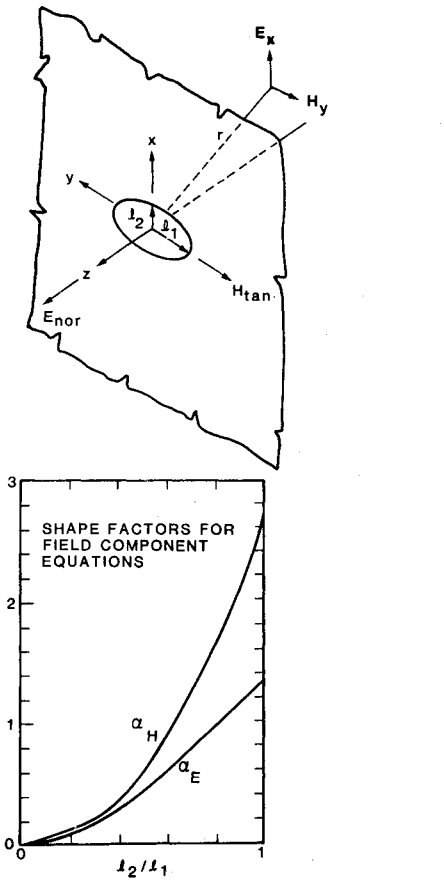

Fig. 11 Shape factors for field component diffraction through an elliptical aperture in an infinite perfectly conduting sheet (from Ref. 30).

Coupling to Antennas

This section provides methods of estimating ECEMP coupling to antennas on spacecraft. Two simple geometries are employed to represent a number of antennas of interest: the monopole and the loop. These antennas may be deliberate or inadvertent. See Ref. 32 for a helpful discussion deliberate antenna types found on aircraft. Examples of inadvertent antennas are the magnetic field-sensitive loop which results from pigtail grounding of a (moderately) shielded cable, or the loop between a solar panel boom and a power cable which may run along it.

Monopole Response

A simple monopole antenna feeding through a dielectric penetration into a transmission line of characteristic impedance Z_c is illustrated in Fig. 12. The antenna is driven by the incident electric field rate of change and by the knock-on

current which is the flux of blowoff electrons intercepted by the monopole cross section. Also shown in the figure is a simple equivalent circuit model of the structure with expressions for estimating the circuit elements. The expressions are greatly simplifed although they provide reasonable estimates of effects when compared with detailed numerical simulations. A more complete analysis of the monopole including experimental data is found in Ref. 33.

Using the simple expressions of Fig. 12 and assuming monopole height and radius 10 cm and 0.5 cm and a gap radius of 1.5 cm, the circuit elements are estimated to be $L \simeq 60$ nH and $C \simeq 3$ pF. Referring to the example calculation for object charge-up time during a dielectric discharge [Eq. (3)], a 2-mil Kapton discharge is seen to cause a length ≃ diameter cylinder to charge to 13 kV in time $T_W \simeq 100$ ns. Ignoring knock-on current, the total current across C in Fig. 12 is $I = C\dot{V} = Eh/T_W \simeq 0.08$ A, where the electric field at the monopole has been estimated by $E = V/R$ with $R = 0.5$ m. This current flows virtually unimpeded through the load due to the small L and C values and the long ECEMP pulse.

Loop Response

The reponse of a loop antenna is $V_{oc} = \dot{B}A$ where V_{oc} is the open-circuit voltage, $\dot{B}$ the incident magnetic induction rate of rise, and A the area of the loop. Assuming a small circular loop, the voltage is $V_{oc} = \mu_0 \dot{H} \pi R^2$ where μ_0 is the permeability of free space and $\dot{H}$ the magnetic field rise rate.

As an example of the loop antenna EMI response, consider the discharge of a 0.8-m^2 Mylar sample caused by a laboratory 25-keV monoenergetic source. According to Table 1, a peak blowoff current of $I_p = 1150$ A flows off the material with a 1.3-μs pulse rise time. If the entire current arcs across a gap of length $h = 5$ mm to ground at a distance of $r = 0.1$ m from the loop with a linear rise pulse, then by differentiating Eq. (9) for H, the field at the loop is

$$\dot{H} = \frac{h}{4\pi} \frac{I_p}{T_R r^2} \simeq 3.5 \times 10^7 \text{ A/m/s} \tag{46}$$

The second term in Eq. (9) has been ignored because $cT_R \gg r$ in this example. If the radius of the loop is $R \simeq 1$ cm, the voltage induced in it is

$$V_{oc} = \mu_0 \dot{H} \pi R^2 \simeq 1.4 \times 10^{-2} \text{V} \tag{47}$$

Such a signal would probably be inconsequential on most systems, but this example involves a very small loop.

Coupling to Cable Shields

ECEMP-induced cable signals can be imagined to result from four separate drivers:

1) Knock-on current (emitted electrons captured by the cable).
2) Magnetic field coupling ($\dot{B}A$ voltage source).
3) Electric field coupling ($C\dot{V}$ current source).
4) Direct drive.

These mechanisms are defined and discussed in the following sections. They are fairly well understood, so the objective here is to a provide simple means to estimate magnitudes of cable responses due to different ECEMP pulses.

In this discussion, the word "cable" can mean the conductor of an unshielded cable, the conducting sheath of a shielded cable, or the outer conducting shield around a cable bundle. The currents estimated are the total currents on the cables or cable shields. The penetration of current through the shield of a single cable or a cable bundle is discussed in a later section.

A summary of cable sheath and direct drive current expressions developed in the following sections for the coupling modes above is given in Fig. 13 for the common low-impedance termination. The cable geometry parameters are illustrated in the upper right, and it is assumed that the cable is near a ground plane. The total cable length is ℓ, its radius a, and its height above the plane is h.

Knock-on Current

Knock-on current is the net flux of electrons captured or emitted by the outside of a cable. Emission by the cable corresponds to a discharge of its dielectric jacket. The emitted current must flow back to ground, mainly through the cable shield, but some small fraction of it will couple into the center conductor of the cable. For worst-case estimates it is conservative to consider the captured and emitted currents separately, since they always produce cable currents of opposite signs.

For the worst-case emitted current, the current per unit length of cable can be taken as the circumference of the cable times the stored charge per unit area released from the cable divided by the dielectric material characteristic discharge pulsewidth (FWHM). Also for worst case, the emission current from the cable can be estimated ignoring space-charge limiting from the cable.

Magnetic Field Coupling

A major coupling mechanism is the voltage induced in a conducting loop by the rate of change of the magnetic flux lines enclosed by that loop. Consider a cable with the centerline above a conducting surface, h, and the length ℓ defining the coupling area ($A = h\ell$). If the cable is close to a surface, the driving B field is the one due to the returning skin current, K_s (A/m).

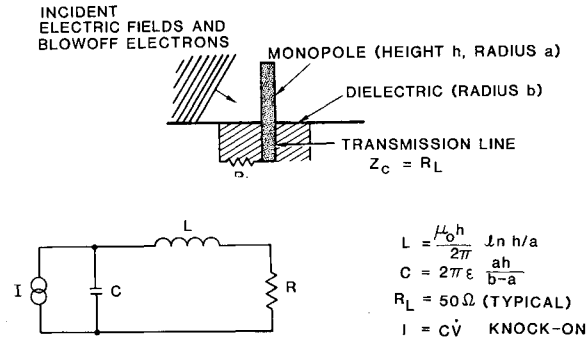

Fig. 12 Simplified lumped-element equivalent circuit representation of a monopole antenna for coupling analysis.

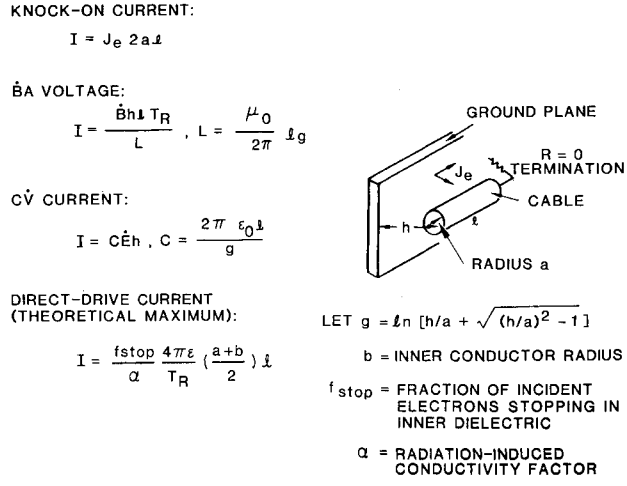

Fig. 13 Summary of cable current expressions for low-impedance terminations for a dielectric discharge rising to a peak emission current density J_e in time T_R.

$$\dot{B}A = \mu_0 A \frac{dK_s}{dt} \tag{48}$$

For $\dot{B}A$ coupling due to the transmitted current in a conducting cavity, it is conservative to assume that the depth of the cavity is small for present purposes so that space-charge limiting will be minimal. Assuming that this cavity is a cylindrical can of radius R, which has a discharging dielectric on one end, the maximum magnetic field H will be adjacent to the cylindrical wall and will have a magnitude

$$H = J_e(R/2) \tag{49}$$

where J_e is the internal emission current density (A/m^2) from the end of the cylinder. The resulting $\dot{B}A$ voltage is

$$\dot{B}A = \mu_0 A \dot{H} = \mu_0 A \frac{R}{2} \frac{dJ_e}{dt} \tag{50}$$

The amount of current that will flow on the cable as a result of the $\dot{B}A$ voltage will depend on its inductance L and its termination resistance Z_R. For a simple circuit with L and Z_R in series (Fig. 14a) and driven by a step voltage $\dot{B}A$, the resulting current in the cable is

$$I(t) = \frac{\dot{B}A}{Z_R}[1 - \exp(-tZ_R/L)] \tag{51}$$

For a large value of Z_R, the exponential term damps out before the driving voltage ($\dot{B}A$) decays away. In that case, the peak I is just $\dot{B}A/Z_R$. However, for essentially short-circuit conditions ($Z_R \simeq 0$), the current I will increase linearly with time for the duration of the voltage driver (t_p), so the peak current is

$$I_p = \frac{\dot{B}At_p}{L} = B_{max}A/L \tag{52}$$

for a constant $\dot{B}$. The inductance L is obtained from the expression in Fig. 13.

Electric Field Coupling

Another major coupling mechanism is electric field coupling into a cable. When the voltage V between two conductors changes with time, the resulting driver for an equivalent electrical circuit can be represented by a current source $C\dot{V}$, where C is the capacitance between the conductors. $\dot{V}$ can be obtained from the local surface electric field near the cable.

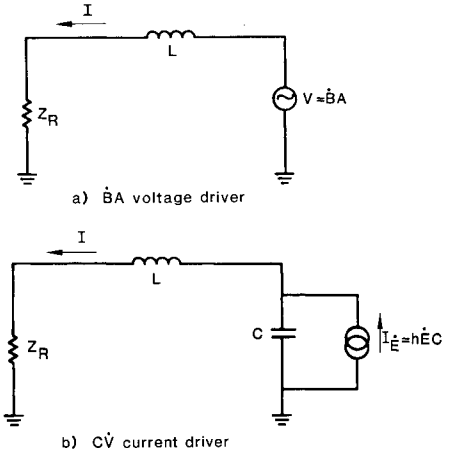

Fig. 14 Simplified equivalent circuit representation of short cables excited by ECEMP discharges.

For a case in which the spacecraft ground moves from a zero potential to a high positive value V due to the discharge of an external dielectric, for example, the field near the cable may be obtainable from the simple expression $E = V/R$, where R is a characteristic dimension of the object. For some cases R may be simply a local radius of curvature.

Assuming that the peak value of the rate of change of the surface electric field $\dot{E}$ is known, the worst-case $\dot{V}$ is just $\dot{E}h$ (see Fig. 13). The capacitance is also given in the figure.

For the simple circuit shown in Fig. 14, the current I in the cable due to a step current driver $h\dot{E}C$ is

$$I(t) = A_1 \exp(-s_1 t) + A_2 \exp(-s_2 t) + h\dot{E}C \tag{53}$$

where

$$S_{1,2} = 0.5(Z_R/L) \pm \sqrt{(Z_R/L^2 - 4C/L}} \tag{54}$$

and A_1 and A_2 are constants determined by the boundary conditions.

If the duration of $\dot{E}$ is long compared to the damping times $1/s_1$ and $1/s_2$, the peak current in the cable will be the steady-state value $h\dot{E}C$. However, if R is very large, the current equation becomes

$$I(t) \simeq h\dot{E}C\{1 - \exp[-t/(Z_R C)]\} \tag{55}$$

so $I(t)$ initial increases linearly as

$$I(t) \simeq h\dot{E}t/Z_R \tag{56}$$

and the peak current is

$$I_p = hE_{max}/Z_R \tag{57}$$

Cable Direct Drive

Discharges directly within cables are treated here caused by 1) bulk dielectric breakdown, and 2) isolated conductor effects.

Bulk Dielectric Breakdown

The problem of predicting the cable response to the bulk breakdown of inner dielectric stored charge is not analytically solvable due to the stochastic nature of the breakdown process and its dependence on complex geometrical factors. It is at least theoretically possible to predict whether a discharge will occur in a given cable however, and to predict the maximum possible response. The method of predicting these unwanted signals is outlined below. The discussion is a brief recap of the approach developed in Ref. 2.

Charge can accumulate in cable dielectrics exposed to electron fluxes sufficiently energetic to penetrate the cable shield. The rate at which charge accumulates depends upon the rate at which electrons are deposited in the dielectric and the rate at which they migrate to the dielectric-metal interface through various conduction processes. The total charge density accumulating in a dielectric depends upon the balance between these two competing processes. An estimate of the charge accumulation can be made by considering a one-dimensional dielectric slab (Fig. 15) sandwiched between two conducting plates, connected through a resistance R, and separated by a distance a.

A flux of electrons is incident from the left with current density J_{inc}. The current strikes the metal plate representing the outer cable shield and is attenuted by the metal such that a current density J_i is incident on the dielectric slab representing the cable dielectric. The electron current is further attenuated by the dielectric such that a current density J_0 exits the dielectric into the conductor at the right, representing the cable center core.

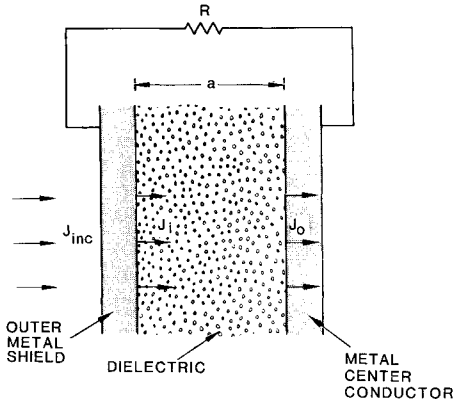

Fig. 15 One-dimensional slab representing dielectric sandwich between outer cable shield and center conductor.

The accumulation of charge in the volume is governed by the continuity equation which in steady state balances the electron environment penetrating current with the radiation conductivity-induced conduction current. The saturation electric field which results is

$$E_{\text{sat}} = \frac{J_i - J_0}{(J_i + J_0)\alpha} = \frac{f_{\text{stop}}}{\alpha} \tag{58}$$

where α is the radiation-induced conductivity factor in the expression $\sigma = \alpha J$, where σ is the conductivity. Experimental values of α are available for several satellite materials.

The quantity f_{stop} is the fraction of the incident electron current which actually stops in the dielectric compared to the average current in the bulk. It can be obtained from the charge deposition profile in the cable materials. This profile may be calculated accurately using a detailed electron transport code such as SANDYL, or may be approximated by the simple method of assigning each element of charge in the incident spectrum to a location in the bombarded materials corresponding to the practical electron range for the energy of the element. The latter method was employed using incident natural and nuclear spectra based on measured natural environments and a typical fission spectrum. Resulting charge deposition profiles are shown in Fig. 16. The profiles employed the simple electron range-energy relationship corresponding approximately to $\tau = \rho R = 2.4 \times 10^{-4}\ (\mathcal{E}/10)^{1.82}$ where τ is in g/cm^2 and $\mathcal{E}$ is in keV. Curves are presented for two bounding assumptions regarding the location of electron deposition: 1) all the electrons stop at the practical range, and 2) the electrons in each initial energy bin deposit uniformly over their practical range in the material. The form of the data in Fig. 16 allows the value of f_{stop} to be obtained by the expression

$$f_{\text{stop}} = \frac{f_o - f_i}{2 - (f_o + f_i)} \tag{59}$$

where f_i is the fraction of the total spectrum stopped immediately before it reaches the dielectric and f_o the fraction of the total spectrum stopped immediately after the dielectric. The values of f_i and f_o are read directly off the graphs for each penetration depth.

As an example calculation, consider satellite cables which consist of an outer copper shield of thickness 0.26 g/cm^2 and a center Teflon dielectric of 0.23 g/cm^2 (radially). From Fig. 16, it can be estimated that the fraction of electrons in the natural environment stopped before reaching the Teflon is ~0.6 (using the deposition at the practical range curve), and the fraction of the total spectrum stopped by the radial location corresponding to the edge of the Teflon at the center conductor is ~0.8. The fraction stopped compared to the average current in the Teflon by Eq. (59) is $f_{\text{stop}} \simeq 0.3$, and the saturation field by Eq. (58) is $E_{\text{sat}} = f_{\text{stop}}/\alpha \simeq 2.3 \times 10^5$ V/cm. The value employed for α is based on experimental measurements of conductivity per unit dose and calculations of dose per electrons per cm^2 (described in Ref. 2). The electric field which results is just above the Teflon breakdown value of 2×10^5 V/cm. Thus, it is concluded that spontaneous breakdowns are possible in this cable type.

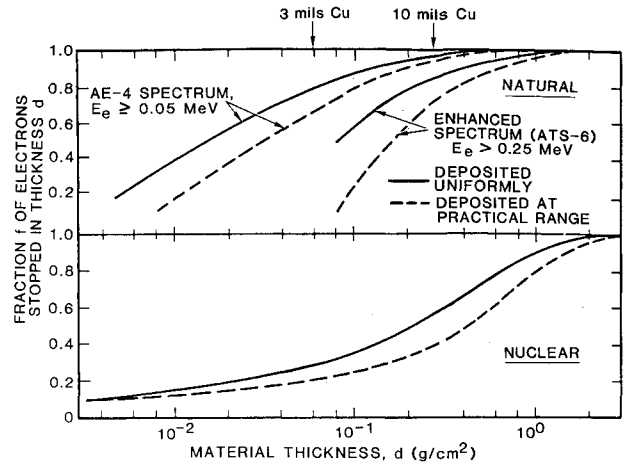

Fig. 16 Integral electron deposition profiles.

Given that a breakdown may occur, it is straightforward to estimate the worst-case current which can flow. That current is

$$I = \rho_{\text{sat}} \pi (r_o^2 - r_i^2) \ell / T_W \tag{60}$$

where ρ_{sat} is the saturation charge density (assumed uniform throughout the dielectric, r_i and r_o are the inner and outer dielectric radii, respectively, ℓ the cable length, and T_W the discharge current pulse FWHM. The saturation charge density can be obtained from

$$\rho_{sat} \simeq \frac{2\epsilon E_{\text{sat}}}{r_o - r_i} \tag{61}$$

where E_{sat} is as described above. The pulse time T_W must be estimated from experimental observations of discharges in cables since no useful theories of the process exist at present. A value of 50 ns for a 1-m cable length has been employed based on monoenergetic electron illumination of one cable type in a JAYCOR experimental program. Using dielectric inner and outer radii of 0.046 and 0.149 cm, respectively, for the Teflon-dielectric cables, the current per unit length is $I/\ell \simeq 44$ A/m by Eq. (60). The experimental measurements were considerably below this level (≤ 2 A/m maximum) indicating a relatively small fractional participation of the stored charge in any given discharge.

Isolated Conductor Discharges

An unused wire in a cable may accumulate charge up to the breakdown point. For a thin dielectric jacket of a few mils, a buildup on the isolated wire of $V \simeq 1$ kV may be sufficient to exceed the dielectric strength depending on proximity of grounded conductors. As an example of the induced response, consider a wire inside a braid in which the average spacing between the isolated wire and the shield is approximately equal to the shield radius. Then the capacitance per unit length is $C/\ell \simeq 2\pi\epsilon$ and the discharge current per unit length is $I/\ell \simeq C/\ell V/T_W$. For a relative permittivity of 4 and a pulsewidth of 50 ns per the JAYCOR measurements, the current flow is approximately 5 A/m of cable length.

Coupling Through Cable Shields

Currents and voltages which appear on cable shields due to external signal penetration or internal discharges penetrate the shields to a certain extent and induce unwanted signals on the internal conductors. The ability of the signals to penetrate is a function of the incident signal parameters and the quality of the shield for those parameters. Shield quality can be quantified by the cable transfer admittance and impedance, and considerable effort has gone into characterizing these quantities over broad ranges of frequency for important cable types.[34-37]

Sheath Transfer Admittance and Impedance

The transfer admittance Y gives the efficacy of voltage between the sheath of a cable and structure ground to induce a current on the center conductor regardless of any other coupling mechanism. Similarly, the transfer impedance Z gives the efficacy of a current on the sheath to induce a voltage on the center conductors. Y and Z are employed to determine cable center conductor signals I and V from the sheath signals I_0 and V_0 by $I = YV_0$ and VI_0.

Based on Refs. 34 and 35, values for these quantities are obtained from

$$Y = j\omega C_{12}\ell_c \tag{62}$$

$$Z = (R_1 + j\omega M_{12})\ell_c \tag{63}$$

where R_1 is a dc diffusion resistance per unit length, C_{12} and M_{12} represent electric and magnetic field coupling through apertures in the braid, respectively, ω the driver frequency in rad/s, and ℓ_c the total cable length. The resistance, capacitance, and inductance constants are highly cable-dependent. Values for typical cables with poor shields are $R_1 = 0.1\Omega/\text{m}$, $C_{12} = 3\times10^{-12}\text{F/m}$, and $M_{12} = 10^{-9}$ H/m. Values for $|Y|$ and $|Z|$ are in mhos and ohms, respectively, and are dependent on the sheath signal frequencies. Typical values for an ECEMP pulse of 200-ns FWHM are 6×10^{-7} mho for admittance during the sheath voltage formation, and 0.1 Ω for impendance during the sheath current buildup (per meter of cable length).

The above expression can be employed for many cable types, but agreement with experimental data is not entirely satisfactory. Madle[37] has asserted that the lack of correlation which exists for certain cable types is due to a weave characteristic known as "porpoising" in which inadvertently unbonded wires in the braid can pick up magnetic field-induced voltages and transport them to the interior. The expressions above do not account for this cable braid property because they are based on aperture leakage models. Some experimental transfer impedance cable data are presented in the following section on measured transfer functions to help circumvent this problem for a few cable types.

Connector Leakage

Leakage of external signals through connectors is a major EMI source. This may be the major source of penetration for doubly braided cables for frequencies ranging through those of interest to ECEMP and higher for standard connectors. High-quality connectors (those thought sufficient for missile applications) have leakage corresponding to less than 10 cm of singly braided cable. Reference 37 presents results of measurements which show that typical connectors cause more leakage above 1 mHz than 40 cm of RG-141 cable.

Measured Transfer Functions

There exists a body of experimental data for transfer functions relating currents and fields on one part of a vehicle to currents and fields on other parts.[37,38] The use of measured transfer functions has the advantage of bypassing many of the approximations of the several analysis steps outlined in Fig. 2.

Table 3 Maximum cable transfer impedances (corresponding to maximum leakage) in the frequency range 0.1-100 M Hz for several cable types based on the measurements of Madle[37]

Cable type	$20\log_{10}(Z_{tr}/50)$[a]	Shield construction
F-182	−58	Thin solid brass
RG-400U	−83	Double braid
SF-400	−80	Triple braid
RG-141	−85	Solid tubular copper
RG-58 C/U	−40	Single braid
RG-174/U	−45	Single braid
RG-58/U	−51	Single braid
RG-223/U	−86	Double braid

[a] Z_{tr} is the transfer impedance in Ω/m.

Table 4 Effects of EMP-induced currents on electronic components (from Ref. 39)

Coupled energy, J	Possible damage
10^{-9}-10^{-8}	Digital upset
10^{-7}	Microwave mixer diodes burnout
10^{-6}	Linear IC's suffer upset and burnout
10^{-5}	Low-power transistors and bipolar IC's upset and burnout
10^{-4}	CMOS logic, medium power transistor, diodes, and capacitors suffer permanent damage
10^{-3}	Zeners, SCR, JFET's, high-power transistor, and thin film resistors damaged

They are particularly well defined when the external field coupling path is well known. In the case of the STARSAT measurements,[38] the solar panel boom penetration was thought to be such a well-defined point of entry. When pin response currents were normalized to fractions of this current during injection tests, a value of 10^{-4} was found to be typical. Combining this transfer coefficient with the 100-A boom current for FLTSATCOM based on scaled experiments (Fig. 3), a current of 10^{-2} A results at the pins (which would cause 0.5 and 10 V signals in 50 and 1000 Ω circuits, respectively).

Direct measurement results of shielding attenuation of several cable types are found in Ref. 37. The results are presented over a broad range of frequencies in that article. They are summarized in terms of maximum cable leakage found in the frequency range 0.1-100 MHz of interest for ECEMP in Table 3. The values found there should provide the analyst with conservative worst-case estimates of shield leakage based on the measurements. The leakage is dominated by the transfer impedance for most practical cases.

Box Discharges

Another source of electrical interference arises from discharges which can occur within the electronic boxes themselves. The charging results from the high-energy component of the electron environment that penetrates the spacecraft exterior and electronic box wall, and deposits charge onto dielectrics and isolated conductors within the box. Typical minimum material thicknesses between the exterior and the electronics are on the order of 80 mils which corresponds to an electron range for 1.3 MeV particles.

Discharges within the box occur only when the incident flux is sufficiently high such that the rate of charging exceeds the rate of leakage through or on the dielectric's surface. Numerous measurements have been made to determine this minimum flux. The minimum flux is somewhat dependent upon the specific materials and configurations, but, in general, is in the range of 10^6-10^7 e/cm^2/s. Below these levels, spontaneous discharges have not been observed, while above

these levels discharges are observed generally on those configurations and materials for which discharges are understood to be feasible theoretically.

Discharges within the box can result from both charged dielectrics and charged isolated conductors. The description of charging and discharging of dielectrics within the box is essentially the same as for other dielectrics elsewhere on the spacecraft. Charging of isolated conductors is addressed in more detail here. Typical isolated pieces of metal found in spacecraft boxes include: unused lands, spot shields, screws and fasteners, board stiffness, relay cases, piece-part lids, and logos. In addition to isolated metal in the boxes, there may be isolated metal elsewhere on the spacecraft in close proximity to electronics such as unused wires in cable bundles.

The discharge characteristics from isolated metals depend upon the geometry and configuration. The discharge may flow along the surface of a PC board as charge may be blown off the isolated metal to other nearby conductors or to the box wall. Discharge characteristics are also affected by whether or not the isolated metal is coated with dielectric such as the case of an unused land on a conformally coated PC board.

Simple estimates of the voltages, currents, and energies involved in a discharge can be made as follows. The amount of charge involved in a discharge or from metal area A is $Q=\sigma_c A$, where σ_c is the accumulated charge density required to initiate the discharge. Typically the minimum charge density is on the order of 10^{-7} C/cm^2. Typical ungrounded PC board areas are 1-2 cm^2 so that the total charge is typically 10^{-7} C.[9]

The peak current I_p from such a discharge is $I_p \simeq Q/T_W$, where T_W is the pulsewidth of the discharge. The pulsewidth depends upon the type of discharge (surface vs blowoff) and the box dimensions. Typical measured pulsewidths in boxes are on the order of 50 ns. Corresponding peak currents could be as high as $I_p \sim 2$ A. No direct measurements of the discharge currents have been made but currents coupled into 50-Ω leads in nearby lands have exceeded 100 V or over 2 A. Thus peak discharge currents of 2 A are not unreasonable for 1-2 cm^2 isolated conductor areas.

The energy involved in the discharges is on the order of $W=\frac{1}{4}I_p^2 Z T_W$. Energies measured in 50-Ω leads have been in excess of several microjoules. The energy delivered to piece parts could be much larger than this for larger land areas, larger minimum accumulated charged needed for breakdown, or higher coupling to piece parts.

Coupled Electromagnetic Energy Upset and Burnout Levels

The estimates of current and voltage signals received at electronics boxes due to the processes described herein can be put in perspective by using them to estimate coupled energy and comparing the results with typical electronic component upset and burnout levels. The coupled energy to a circuit of characteristics impedance Z is

$$W=\int I^2 Z dt \sim \frac{I_p^2 Z T_W}{4} \tag{64}$$

where I is the ECEMP-induced current in the circuit, I_p the peak current, and T_W the pulse FWHM of that current. Typical values for Z are between 50 and 1000 Ω for radio frequency and digital circuits.

Table 4 gives some typical burnout and upset energy levels for electronic components for EMP-induced signals. Since EMP-induced signals contain much of the same frequencies as ECEMP signals, the values in the table can be used for estimates of ECEMP-induced problems. The values shown are gross approximations. In general, the low-power, high-speed, narrow-junction, low-saturation devices are most susceptible to EMI upset or burnout, and this is reflected in the table. The larger power devices are considerably less susceptible.

References

[1]Rosen, A., "Spacecraft Charging by Magnetospheric Plasmas," *IEEE Transactions on Nuclear Science,* Vol. NS-23, Dec. 1976, pp. 1762-1768.

[2]Wenaas, E.P., "Spacecraft Charging Effects by the High-Energy Natural Environment," *IEEE Transactions on Nuclear Science,* Vol. NS-24, Dec. 1977, pp. 2281-2284.

[3]De Plomb, E.P., and Rich, W.F., "Charging of Spacecraft by Nuclear Electrons," *IEEE Transactions on Nuclear Science,* Vol. NS-24, Dec. 1977, pp. 2298-2304.

[4]Stevens, N.J. and Roche, J.C., "NASCAP Modelling of Environmental-Charging-Induced Discharges in Satellites," *IEEE Transactions on Nuclear Science,* Vol. NS-26, Dec. 1979, pp. 5112-5120.

[5]Treadaway, M.J. et al., "Experimental Verification of an ECEMP Spacecraft Discharge Coupling Model," *IEEE Transactions on Nuclear Science,* Vol. NS-27, Dec. 1980, pp. 1776-1779.

[6]Woods, A.J. et al., "Model of Coupling of Discharges into Spacecraft Structures," *Proceedings of Spacecraft Charging Technology Conference,* Colorado Springs, Colo., Nov. 1980, AFGL-TR-81-0270, 1981, pp. 745-754.

[7]Woods, A.J. and Wenaas, E.P., "ECEMP Discharge Modeling," AFWL-TR-81-92, Aug. 1979.

[8]Flanagan, T.M. et al., "Effect of Laboratory Simulation Parameters on Spacecraft Dielectric Discharges," *IEEE Transactions on Nuclear Science,* Vol. NS-26, Dec. 1979, pp. 5134-5140.

[9]Wenaas, E.P., Treadaway, M.J., Flanagan, T.M., Mallon, C.E., and Denson, R., "High-Energy Electron-Induced Discharges in Printed Circuit Boards," *IEEE Transactions on Nuclear Science,* Vol. NS-26, Dec. 1979, pp. 5152-5155.

[10]Treadaway, M.J., Mallon, C.E., Flanagan, T.M., Denson, R., and Wenaas, E.P., "The Effects of High-Energy Electrons on the Charging of Spacecraft Dielectrics," *IEEE Transactions on Nuclear Science,* Vol. NS-26, Dec. 1979, pp. 5102-5106.

[11]Hoge, D.G., "Meteosat Spacecraft Charging Investigation," *Proceedings of Spacecraft Charging Technology Conference,* Colorado Springs, Colo., Nov. 1980, AFGL-TR-81-0270, 1981, pp. 814-834.

[12]Reddy, J., "Electron Irradiation Tests on European Meteorological Satellite," *Proceedings of Spacecraft Charging Technology Conference,* Colorado Springs, Colo., Nov. 1980, AFGL-TR-81-0270, 1981, pp. 835-855.

[13]Balmain, K.G., and Dubois, G.R., "Surface Discharges on Teflon, Mylar, and Kapton," *IEEE Transactions on Nuclear Science,* Vol. NS-26, Dec. 1979, pp. 5146-5151.

[14]Hazelton, R.C. et al., "Measurements of Particle Emission from Discharge Sites in Teflon Irradiated by High-Energy Electron Beams," *IEEE Transactions on Nuclear Science,* Vol. NS-26, Dec. 1979, pp. 5141-5145.

[15]Higgins, D.F., "Analytic Calculations of the Electromagnetic Fields from a Highly Space-Charge-Limited SGEMP Boundary Layer," AFWL Theoretical Note 286, Aug. 1976.

[16]Katz, I., et al., "A Theory of Dielectric Surface Discharges," *IEEE Transactions on Nuclear Science,* Vol. NS-27, Dec. 1980, pp. 1786-1791.

[17]Balmain, K.G., and Hirt, W., "Dielectric Surface Discharges: Effects of Combined Low-Energy and High-Energy Incident Electrons," *Proceedings of the Spacecraft Charging Technology Conference,* Colorado Springs, Colo., Nov. 1980, AFGL-TR-81-0270, 1981, pp. 115-128.

[18]Koons, H.C., "Aspect Dependence and Frequency Spectrum of Electrical Discharges on the P78-2 (SCATHA) Satellite," *Proceedings of the Spacecraft Charging Technology Conference,* Colorado Springs, Colo., Nov. 1980, AFGL-TR-81-0270, 1981, pp. 478-492.

[19]Newell, D.M. and Waters, W.E., "Spacecraft Charge Protection of Large Three-Axis-Stabilized Communications Satellites – INTELSAT V Design," *IEEE Transactions on Nuclear Science,* Vol. NS-28, Dec. 1981, pp. 4545-4508.

[20]Tumolillo, T.A. and Wondra, J.P., "MEEC-3DP: A Computer Code for the Self Consistent Solution of the Maxwell-Lorentz Equations in Three Dimensions," *IEEE Transactions on Nuclear Science,* Vol. NS-24, Dec. 1977, pp. 2249-2455.

[21]Stettner, R., and Longley, H.J., "Description of the SGEMP Computer Code: SEMP," DNA 3909T, June 1975.

[22]Woods, A.J., and Delmer, T.N., "The Arbitrary Body-of-Revolution Code (ABORC) for SGEMP/IEMP," DNA 4348T, July 1976.

[23]Mandell, M.J. et al., "Calculation of Surface Current Response to Surface Flashover of a Large Sample Under Grounded and Floating Conditions," *Proceedings of the Spacecraft Charging*

Technology Conference, Colorado Springs, Colo., Nov. 1980, AFGL-TR-81-0270, 1981, pp. 730-744.

[24]Seidler, W.A. et al., "Investigation of Enhanced Electron Current Transport in a Dielectric-Lined Cavity," *IEEE Transactions on Nuclear Science,* Vol. NS-26, Dec. 1979, pp. 4998-5005.

[25]Stettner, R. et al., "Physical Modelling of Spacecraft Discharge Processes and Associated Electron Blowoff," *IEEE Transactions on Nuclear Science,* Vol. NS-27, Dec. 1980, pp. 1780-1785.

[26]Mandell, M.J. et al., "Mechanism for SGEMP-Triggered Surface Flashover," *IEEE Transactions on Nuclear Science,* Vol. NS-26, Dec. 1979, pp. 5030-5034.

[27]Butler, C.M. et al., "Selected Topics in EMP Interaction," AFWL EMP Interaction Note 339, Aug. 1976.

[28]Butler, C.M. et al., "Electromagnetic Penetration through Apertures in Conducting Surfaces," *IEEE Transactions on Electromagnetic Compatibility,* Vol. EMC-20, Feb. 1978, pp. 82-93.

[29]Taylor, C.D., "Electromagnetic Pulse Penetration Through Small Apertures," EMP Interaction Note 74, AFWL TR-73-67, March 1973.

[30]Merewether, D.E. et al., ed., "Electromagnetic Pulse Handbook for Missiles and Aircraft in Flight," Sandia Rept. SC-M-71-0346, AFWL-TR-73-68, Sept. 1972.

[31]Madle, P.J., "Transfer Impedance and Transfer Admittance Measurements on Gasketed Panel Assemblies, and Honeycomb Air-Vent Assemblies," *IEEE Electromagnetic Compatibility Symposium Record,* 1976, pp. 204-209.

[32]Lee, K.S.H., Lin, T.K., and Marin, L., "EMP Response of Aircraft Antennas," *IEEE Transactions on Electromagnetic Compatibility,* Vol. EMC-20, Feb. 1978, pp. 94-99.

[33]Stettner, R. et al., "SGEMP Response Investigations with Exploding-Wire Photons, Part II," *IEEE Transactions on Nuclear Science,* Vol. NS-25, Dec. 1978, pp. 1342-1348.

[34]Higgins, D., "SGEMP Leakage Through Satellite Cable Shields: The Importance of Transfer Admittance Coupling and Its Implications on Testing," *IEEE Transactions on Nuclear Science,* Vol. NS-27, Dec. 1980, pp. 1589-1593.

[35]Vance, E.F., *Coupling to Shielded Cables,* John Wiley & Sons, New York, 1978.

[36]Casey, K.F., Vance, E.F., "EMP Coupling Through Cable Shields," *IEEE Transactions on Electromagnetic Compatibility,* Vol. EMC-20, Feb. 1978, pp. 100-106.

[37]Madle, P.J., "Cable and Connector Shielding Attenuation and Transfer Impedance Measurements Using Quadraxial and Quintaxial Test Methods," *IEEE Electromagnetic Compatibility Symposium Record,* pp. 4BIb1-b5, 1975; also, private communication, Jan. 1983.

[38]Seidler, W., Wondra, J., and Walters, D., "High-Level Current Injection Testing of the SGEMP Test, Analysis and Research Satellite (STARSAT); *IEEE Transactions on Nuclear Science,* Vol. NS-28, Dec. 1981, pp. 4211-4220.

[39]Hastings, C.R., Demaris, E.E., and Rose, M.A., "Development and Production of Nuclear Hardened Weapon Systems," paper presented at Fourth Vulnerability and Survivability Symposium, Tyndale AFB, Panama City, Fla., March 14, 1979, sponsored by the American Defense Preparedness Association.